Optimizing PV–Battery Hybrid Systems: A Reconfigurable Approach With Module-Level Maximum-Power-Point Tracking and Load Sharing

Wei Jiang, Nima Tashakor, *Member, IEEE*, Pouyan Pourhadi Abkenar, Alexander Koehler,
Hui Wang, *Member, IEEE*, and Stefan M. Goetz, *Member, IEEE*

***Abstract*—This article presents a novel hybrid reconfigurable battery and photovoltaic (PV) system designed to meet the growing demand for efficient renewable energy sources. The system features a modular reconfigurable architecture with compact coupled inductors and a unique modulation strategy, which enhance flexibility and energy utilization. The system ensures that each PV component operates at its maximum power point (MPP) to maximize power generation, while it solves the problems of hard-wired connections, such as local optima and scalability. The battery module seamlessly adapts to fluctuations in PV power output and load demands, while it ensures a stable dc-bus voltage output. Intermediate states between parallel and series connectivity are created through coupled inductors to manage voltage differences between paralleled modules. These inductors offer a small footprint and minimal magnetic material usage. They do not need to manage the high common-mode magnetic flux at high load currents but serve for the balancing currents through high differential-mode inductance. The proposed modulation strategy enables efficient bidirectional energy transfer and allows precise control of power exchange between modules independently of output control. The independent control facilitates charge and load balancing between battery and PV panels with varying voltages. Simulations and experiments demonstrate the system's MPP tracking performance with at least 97% efficiency, an approximate 19% increase in energy output compared to a fixed string of two PVs, and $<$1% ripple in the output voltage and current.**

***Index Terms*—Coupled inductor, grid integration, maximum power point tracking (MPPT), photovoltaics (PV), reconfigurable PV–battery structure.**

I. Introduction

IN THE face of climate change, the transition to low-carbon energy sources is crucial. Due to a massive cost drop in the last decades, photovoltaic (PV) panels stand out among green energy solutions. They offer easy installation as well as long-term reliability and contribute significantly to global renewable energy growth [1]. However, to limit global warming to 1.5 °C, renewable energy would need to grow faster and requires enhanced efficiency, reliability, and cost-effectiveness in renewable energy systems [2].

PV generation presents challenges due to its intermittent nature, which can result in voltage and frequency fluctuations in power systems [3], [4], [5]. Battery energy storage systems have emerged to solve these issues [6], [7], [8]. Battery storage ensures grid stability and reliability with the ability to respond rapidly to power needs, supply immediate power deficits, and compensate unforeseen fluctuations [9], [10].

Conventional PV and battery system interconnections via dc–dc converters encounter challenges as systems become larger [11], [12], [13]. Large setups with separate PV and battery units each with their own inverter often connect in parallel to the grid and, thus, require at least three conversion steps for energy transfer, typically even more due to dc–dc conversion and power-point tracking. However, large strings of PV panels with only one central inverter are limited by the weakest element, such as a defective PV module or battery cell or just due to partial shading [7], [14], [15]. The performance spread between elements in a system result in load sharing issues and reduced efficiency and reliability [16], [17], [18], [19]. Flexible and dynamically reconfigurable connections can solve these challenges and optimize system performance in diverse conditions [20], [21].

Cascaded bridges, such as diode-clamped [22], [23], flying-capacitor [24], [25], and modular multilevel converter (MMC) structures [26], [27], [28], are potential solutions for reconfigurable PV systems [29], [30], [31], [32], [33], [34], [35], [36], [37], [38], [39], [40], [41], [42], [43], [44], [45]. Previous attempts to create such systems used diodes, which have

Received 24 February 2024; revised 8 July 2024; accepted 16 August 2024. Date of publication 6 September 2024; date of current version 12 December 2024. This work was supported in part by Anhui Provincial Scientific Research Project under Grant 2024AH040198, in part by Industry Think Tank under Grant ypzk004, in part by the German Federal Ministry for Education and Research (BMBF) within the project under Grant »Open6GHub« 16KISK003K, and in part by KSB Foundation. Recommended for publication by Associate Editor P. Acuna. *(Wei Jiang, Nima Tashakor, and Pouyan Pourhadi contributed equally to this work.) (Corresponding author: Nima Tashakor.)*

Wei Jiang is with the Department of Intelligent Engineering, Bozhou Vocational and Technical College, Bozhou 236800, China, and also with the Department of Electrical and Computer Engineering, Rheinland-Pfälzische Technische Universität,Bozhou Vocational and Technical College, 67663 Kaiserslautern, Germany (e-mail: 0430077005@bzy.edu.cn).

Nima Tashakor, Hui Wang, and Stefan M. Goetz are with the Department of Electrical and Computer Engineering, Duke University, Durham, NC 27708 USA, and also with the Rheinland-Pfälzische Technische Universität, 67663 Kaiserslautern, Germany (e-mail: nima.tashakor@duke.edu; hui.wang@duke.edu).

Pouyan Pourhadi Abkenar and Alexander Koehler are with the Department of Electrical and Computer Engineering, Rheinland-Pfälzische Technische Universität, 67663 Kaiserslautern, Germany (e-mail: pourhadi@eit.uni-kl.de; akoehler@rptu.de).

Color versions of one or more figures in this article are available at https://doi.org/10.1109/TPEL.2024.3455229.

Digital Object Identifier 10.1109/TPEL.2024.3455229

drawbacks including high losses [46], [47]. An optimal reconfigurable PV system should efficiently extract energy from all modules and bring each module to its individual maximum power point (MPP). Research has suggested various reconfigurable PV concepts, e.g., to remove shaded modules from the active string with mechanical relays and route their residual energy to a separate battery [48]. However, control and hardware effort are high for only a low advantage. An alternative introduces a switched-capacitor-based charge redistribution circuit for two-dimensional perturb-and-observe maximum power point tracking (MPPT) [49]. However, this method impairs power conversion efficiency, especially in case of cell mismatch and partial shading. Goetz et al. [20] proposed a topology that separates local power factor correction and storage in the modules. This design uses a fixed ratio of solar energy and storage, which however limits system flexibility and adaptability. Additionally, all solar energy, even if directly fed into the grid, must pass through the local MPPT boost conversion, which increases the number of conversion steps and lowers efficiency.

To simplify control and increase flexibility, some applications incorporate PV panels and batteries into modular structures. A configuration combines PV and battery modules into a double-star cascaded bridge structure to create a multiport reconfigurable PV plant suitable for high-voltage direct-current applications [50]. However, high-voltage systems may encounter common-mode challenges due to the inherently large capacitance in PV modules associated with the panels' physical size, which can lead to significant current flow and safety risks [51], [52], [53]. These systems have drawbacks, including no direct energy exchange between modules, lack of a parallel mode with an impact on utilization, redundant multiple energy-conversion stages, low efficiency, and high cost. Similarly, integrating energy storage and PV modules into MMCs faces similar issues [51], [52], [53]. Additionally, reconfigurable topologies with parallel connections and direct energy exchange often lack compatibility with PV systems and control strategies that suit PV-specific requirements [54], [55], [56], [57], [58], [59], [60].

This article fills this gap by introducing a hybrid system that incorporates both PV and batteries, each in dedicated modules strung together into a system with a double module-interconnection bus. Coupled inductances between modules with corresponding modulation enable voltage-independent direct energy exchange and dynamic power routing, reducing energy conversion stages. Furthermore, the coupled inductances allow MPPT on the module level without a dedicated local dc–dc converter as in previous research [20], [21]. The hybrid system effectively decouples the control of output voltage and the rate of energy exchange between modules. It enables bidirectional energy transfer between heterogeneous modules through an additional mode. Importantly, this energy exchange is achieved independently of the individual module voltages.

Some of the main contributions and advantages of the proposed system are as follows.

1) Minimal output voltage and current ripple ($<1\%$) observed in simulations and experiments due to increased effective switching frequency as well as higher voltage granulation.
2) Intermodule balancing and load-current distribution with the coupled inductor pairs.
3) Ability to operate each PV module at its optimal global MPP and efficiently transfer excess energy to neighboring battery module.
4) Direct energy exchange between PV modules and batteries, eliminating the need for multiple energy conversion stages and reducing conversion losses.
5) Introduction of compact mutual inductances and a corresponding modulation technique to achieve maximum power on the module level, enhancing flexibility in energy transfer and load sharing among modules.
6) Decoupled control of output voltage and energy exchange rates for independent optimization and improved system performance as well as efficiency.

The rest of this article is organized as follows. Section II introduces the proposed topology and operational principles. Section III delves into power distribution between PVs and battery packs to examine the impact of coupled inductors on load current and voltage balance between modules. Section IV provides the design considerations. Sections V and VI employ simulations and experiments to validate the system's performance. Sections VII compares the system with recent work. Finally, Section VIII concludes this article.

II. TOPOLOGY AND OPERATING PRINCIPLE

A. Module Implementation

The proposed topology combines PV arrays with dedicated battery modules and forms the reconfigurable PV-battery structure shown in Fig. 1. The chosen module structure is an asymmetric double half-bridge with four transistors and a differential inductor. This module structure enables various interconnections (parallel, serial, boost) and can actively control current distribution between modules and energy transfer.

The coupled inductor pairs serve two purposes: 1) they combine intermodule energy exchange and 2) the load current transfer in one shared energy backbone. With minimal inductance for the load current path through low common-mode inductance, they offer substantial inductance specifically for the current component responsible for energy exchange between modules through high differential-mode inductance. While the common-mode inductance remains small, it provides the necessary impedance for grid or load connection at the output as well as for control.

The differential-mode inductance, in conjunction with surrounding module transistors, forms an intermodule dc–dc converter. This converter controls balancing current flow and bridges voltage differences between modules, facilitating local MPPT without a dedicated conversion stage. Consequently, the system enables a PV with lower voltage to charge a neighboring battery module with higher voltage, with energy exchange adjustable to zero while evenly sharing the load between modules. Moreover, the system ensures an even distribution of load current

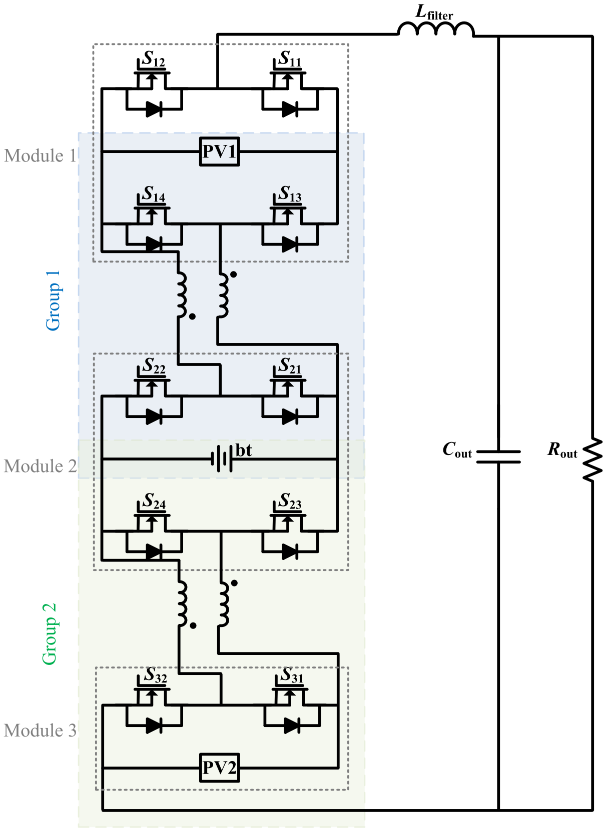

Fig. 1. Configuration of the reconfigurable PV-battery hybrid topology with differential inductors.

among each inductor pair, where currents effectively counteract each other's magnetization.

The dominant inductance, the differential-mode inductance, determines the magnetic core size based on the maximum required intermodule balancing current, typically only a fraction of the load current. This design ensures that each PV module operates at its optimal global MPP, efficiently transferring excess energy to neighboring battery modules. The battery modules can contribute voltage and power to the system's output as needed. These benefits are particularly advantageous in high-power and high-voltage scenarios.

For illustration, we examine an interconnection group that encompasses the lower half-bridge of Module *j*, the upper half-bridge of Module (*j*+1), their respective battery and PV, and the coupled inductor bridging them as a unified unit. Fig. 1 denotes such an interconnection between Modules 1 and 2 as Group 1. Within this configuration, the transistors, in conjunction with the differential-mode inductance, operate as a bidirectional buck–boost dc–dc converter. The dc–dc function operates in tandem with the primary function of these transistors, which is to control the state of module interconnection and manage load current. The coupled inductors are meticulously designed to ensure that the load current (i_{out}), which is evenly divided between the two branches of the coupled inductor (representing the common mode), encounters minimal inductance. Conversely, any variation, such as those induced by balancing currents or the dc–dc modes, all of which contribute to the differential-mode current, faces a substantial inductance. This substantial inductance can be magnetized and demagnetized to facilitate the transfer of current from a lower-voltage module to a higher voltage module or module group [60].

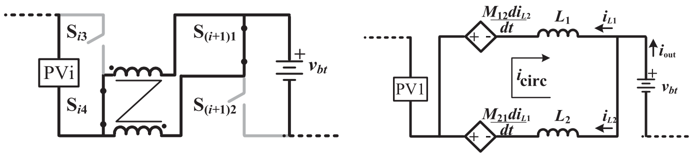

(a) (b)

Fig. 2. (a) Serial mode of asymmetrical double-half-bridge submodules. (b) Equivalent circuit of serial mode.

B. Operation Modes of the Interconnections

While the generation of output voltage and the dc–dc interconnection can be independently controlled, they interact at the transistor level, resulting in a high transistor utilization rate. The utilization for the load current alone reaches 50% and is comparable to that of conventional cascaded bridges or double bridges. On top of that, we further integrated the dc–dc functionality so that the very same transistors simultaneously serve the functions of output formation and intermodule dc–dc operation.

There are three potential operational modes based on the switch states within each interconnection. For the sake of simplicity, we assume that the load current remains relatively constant over one switching cycle. As illustrated in Fig. 2(a), when S_{i4} and $S_{(i+1)1}$ are turned ON, they connect the two modules in series. This mode occurs when the demanded output voltage exceeds the previous level of series-connected modules so that this interconnection also switches to series. The current flowing through the inductors comprises two primary components: one corresponds to i_{out}, while the other pertains to the local circulating current (i_{circ}). When self and mutual inductances are symmetrical ($L_1 = L_2 = M_{12} = M_{21}$), i_{out} is evenly divided between the coupled inductors, while i_{circ} freely circulates between these two inductors. Hence, the inductor currents based on i_{out} and i_{circ} follow:

$$i_{L1} = \frac{i_{\text{out}}}{2} + i_{\text{circ}},\ i_{L2} = \frac{i_{\text{out}}}{2} - i_{\text{circ}}. \tag{1}$$

The number of modules in series determines the output voltage of the string (v_{out}) per

$$v_{\text{out}} = \sum_{x=i} (s_i \times v_i)\,. \tag{2}$$

Variable s_i can be 0 in the parallel and boost modes or 1 in the series mode, where i is the module number. Module voltage v_i can be v_{PV} or v_{bt}. According to (2), all the battery and PV modules can contribute to generating the output voltage. This flexibility is one of the advantages of this topology compared to the ones where the batteries are connected in parallel to the output or PV. Fig. 2(b) presents the equivalent circuit for one

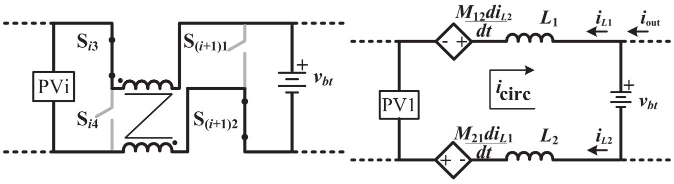

(a) (b)

Fig. 3. (a) Parallel mode. (b) Equivalent circuit of the parallel mode.

set of inductors in the series mode. Based on Fig. 2(b), $i_{\text{out}} = i_{\text{L1}} + i_{\text{L2}}$. Assuming that $L_1 = L_2$, the effective common-mode inductance experienced by i_{out} is

$$L_{\text{eff,CM}} \approx 0.5\ (L_1 - M_{12}) = 0.5\,(L_2 - M_{21}) \approx 0 \tag{3}$$

and the effective differential-mode inductance is

$$L_{\text{eff,DM}} \approx L_1 + M_{12} + L_2 + M_{21} = 2\,(L_1 + M_{12})\,. \tag{4}$$

This can be easily calculated using Kirchhoff's voltage law (KVL) per

$$L_1 \frac{\text{d}i_{\text{L1}}}{\text{d}t} - M_{12}\frac{\text{d}i_{\text{L2}}}{\text{d}t} - L_2\frac{\text{d}i_{\text{L2}}}{\text{d}t} + M_{21}\frac{\text{d}i_{\text{L1}}}{\text{d}t} = 0. \tag{5}$$

Substitution of (1) into (5) results in

$$\Bigl(\underbrace{L_1 + M_{12} + L_2 + M_{21}}_{L_{\text{eff,DM}}}\Bigr)\frac{\text{d}}{\text{d}t}i_{\text{circ}} + \Bigl(\underbrace{0}_{L_{\text{eff,CM}}}\Bigr)\frac{\text{d}}{2\text{d}t}\ i_{\text{out}} = 0. \tag{6}$$

According to (6), the circulating current does not change during the series mode, i.e., $\frac{\text{d}}{\text{d}t}i_{\text{circ}} \approx 0$. By employing the equivalent circuit of the serial mode shown in Fig. 2(b), and applying KVL within the main circuit, v_{out} follows:

$$\begin{aligned} v_{\text{out}} &= v_{\text{PV1}} + \underbrace{\left(-L_1\frac{\text{d}i_{L1}}{\text{d}t} + M_{12}\frac{\text{d}i_{L2}}{\text{d}t}\right)}_{\text{between PV1 and bt}} + v_{\text{bt}} \\ &\quad + \underbrace{\left(-L_1\frac{\text{d}i_{L1}}{\text{d}t} + M_{12}\frac{\text{d}i_{L2}}{\text{d}t}\right)}_{\text{between bt and PV2}} + v_{\text{PV2}} \\ &= v_{\text{PV1}} + v_{\text{bt}} + v_{\text{PV2}}. \end{aligned} \tag{7}$$

The boost mode and parallel mode are specifically created to facilitate bidirectional energy transfer between PVs and the battery. The parallel mode, depicted in Fig. 3(a), can be achieved by manipulating the mentioned switches and activating S_{i3} and $S_{(i+1)2}$. In this mode, (1) still evenly distributes i_{out} (the common-mode current) between the two inductors. However, the rate of change of i_{circ} is contingent on the voltage disparity between the two modules. The parallel mode's equivalent circuit is illustrated in Fig. 3(b) and can be described following:

$$\begin{aligned} v_{\text{PV1}} - v_{\text{bt}} &= L_1\frac{\text{d}i_{\text{L1}}}{\text{d}t} + M_{12}\frac{\text{d}i_{\text{L2}}}{\text{d}t} + M_{21}\frac{\text{d}i_{\text{L1}}}{\text{d}t} - L_2\frac{\text{d}i_{\text{L2}}}{\text{d}t} \\ &= (L_1 + M_{12} + M_{21} + L_2)\frac{\text{d}i_{\text{circ}}}{\text{d}t} \approx 4L_1\frac{\text{d}}{\text{d}t}i_{\text{circ}}. \end{aligned} \tag{8}$$

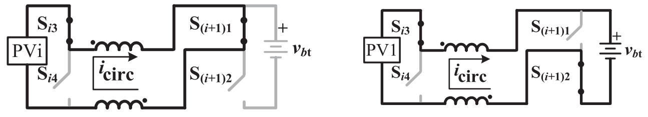

(a) (b)

Fig. 4. Boost mode (left to right). (a) Linearly charging the inductors. (b) Turning to parallel mode.

The effective differential-mode inductance constrains the rate of change of i_{circ} between adjacent modules.

By slightly adjusting the switch toggling times of the two half-bridges, one additional mode could be introduced: the boost mode. Assuming $v_{\text{PV1}} > v_{\text{bt}}$, activated S_{i3}, and $S_{(i+1)1}$ let PV$_i$ charge the coupled inductance [see Fig. 4(a)]. This behavior is akin to a conventional boost converter that comprises an inductor, a switch, a diode, and a capacitor (or in this case, a battery). Consequently, i_{circ} increases in a clockwise direction by discharging PV$_i$, resembling the operation of a conventional boost converter per

$$\begin{aligned} v_{\text{PV1}} &= L_1\frac{\text{d}}{\text{d}t}i_{\text{circ}} + M_{12}\frac{\text{d}}{\text{d}t}i_{\text{circ}} + M_{21}\frac{\text{d}}{\text{d}t}i_{\text{circ}} \\ &\quad + L_2\frac{\text{d}}{\text{d}t}i_{\text{circ}} \xRightarrow{L_1=L_2=M_{12}=M_{21}} \frac{\text{d}}{\text{d}t}\ i_{\text{circ}} = \frac{v_{\text{PV1}}}{4L_1}. \end{aligned} \tag{9}$$

Once the coupled inductors are charged, $S_{(i+1)1}$ and $S_{(i+1)2}$ are, respectively, opened and closed, resulting in a parallel connection in accordance with Fig. 4(b). This demagnetization shifts the energy stored from the coupled inductors to the battery (v_{bt}), which takes on the role of a load in the conventional boost converter. By adjusting the ratio between the duration of the boost mode and the parallel mode, it is feasible to exercise full control over i_{circ} in both directions without any adverse impact on i_{out}. It is important to note that minor timing shifts in the switching of the half-bridges can introduce additional modes, although the effective switching frequency of the half-bridges remains constant.

C. Switching Logic

The switching logic is based on the phase-shifted carrier modulation stated as

$$\text{state } L_{k(k\in\mathbb{N})} = \begin{cases} \text{State 1}: [0\ 1]^T, & m_0 - m_{\text{d2}}\,(m_{\text{d1}}) > C_k \\ \text{State 0}: [1\ 0]^T, & m_0 - m_{\text{d2}}\,(m_{\text{d1}}) < C_k \end{cases} \tag{10}$$

$$\text{state } U_{k(k\in\mathbb{N})} = \begin{cases} \text{State 1}: [1\ 0]^T, & m_0 + m_{\text{d2}}\,(m_{\text{d1}}) > C_k \\ \text{State 0}: [0\ 1]^T, & m_0 + m_{\text{d2}}\,(m_{\text{d1}}) < C_k. \end{cases} \tag{11}$$

C_k represents the kth carrier, while L_k and U_k denote the states of the switches within the upper ($[S_{k3}\ S_{k4}]^T$) and lower

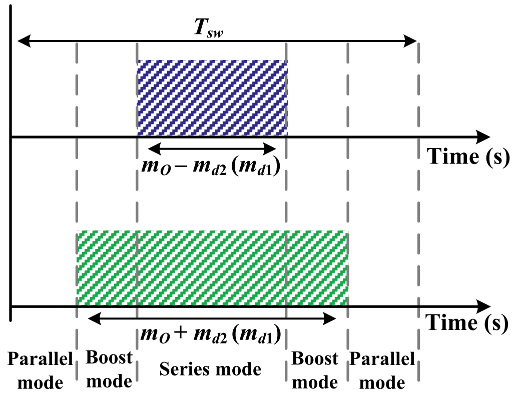

Fig. 5. Half-bridge states (L_k and U_k).

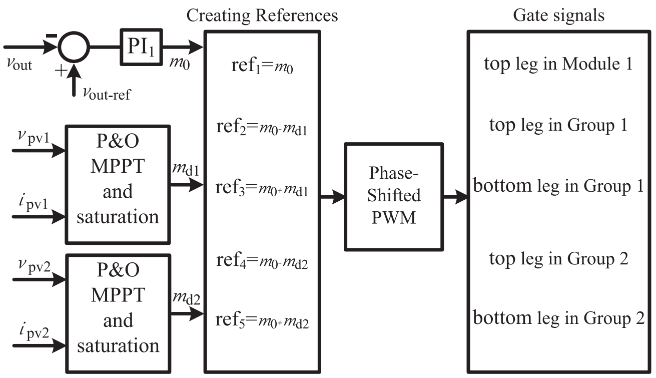

Fig. 6. Control system of the modulation of the groups.

($[S_{(k+1)1}\ S_{(k+1)2}]^T$) half bridges of group k, respectively. Additionally, m_0 and m_{d1} and m_{d2} are control modulation indices responsible for regulating the output voltage and energy transfer between modules. It is worth noting that these controllers can yield both positive and negative values for m_{d1} and m_{d2}.

Fig. 5 presents the states of each half-bridge when m_{d1} and m_{d2} are positive. Specifically, when both the lower and upper half-bridges are in State 1, modules are connected in series, and i_{circ} remains constant. Conversely, when both modules are in State 0, they are connected in parallel, and the circulating current i_{circ} varies according to (9), which means i_{circ} flows from the module with higher to the one with lower voltage. When L_k is in State 0 while $U_k$is in State 1 (i.e., when m_{d1} and $m_{\text{d2}}{>}0$), i_{circ}increases in a clockwise direction. Conversely, when L_k is in State 1 and U_k is in State 0, i_{circ} flows anticlockwise (i.e., when m_{d1} and $m_{\text{d2}}{<}0$). Both of the PVs should work in MPP, and the battery should absorb or make up the difference between the power generated by the PVs and the load. Thus, the controller measures two PV modules' voltage (v_{PV1} and v_{PV2}) and current (i_{PV1} and i_{PV2}) and uses an MPPT algorithm to determine the PV-battery energy interaction references. m_{d1} and m_{d2} are two modulation indices to generate MPPT reference of PV$_1$ and PV$_2$.

As a result, the duration for which the modules are in either series, parallel, or boost states can be determined per

$$\begin{cases} T_{\text{s}} = T_{\text{sw}}\ (m_0 - m_{\text{d2}}\,(m_{\text{d1}}))\,, & \text{Series state}\\ T_{\text{p}} = T_{\text{sw}}\ (1 - m_0 - m_{\text{d2}}\,(m_{\text{d1}}))\,, & \text{Parallel state}\\ T_{\text{b}} = \ \pm 2 T_{\text{sw}} m_{\text{d2}}\,(m_{\text{d1}})\,, & \text{Boost state.}\end{cases} \tag{12}$$

Fig. 6 provides an overview of the control system for our proposed setup. This control strategy can be divided into two largely independent components: one is responsible for regulating the output voltage, denoted as (m_0), and the other focuses on managing the energy transfer between modules. A simple PI controller (PI$_1$) regulates the output voltage and employs a feedback loop to determine m_0. Similarly, a perturb-and-observe algorithm in each interconnection maximizes the individual power points of the PVs.

In the following section, we will provide a more detailed explanation of both the feed-forward and feed-back components of the energy transfer controller.

III. POWER DISTRIBUTION AND ENERGY TRANSFER BETWEEN PVS AND BATTERY

The steady-state circulating current ($i_{\text{circ, SS}}$) due to the voltage difference between the two modules follows:

$$i_{\text{circ,SS}} = \frac{v_{\text{PV1}}\,(i_{\text{PV1}}) - v_{\text{bt}}}{r_{eq}} \tag{13}$$

which can be solved only numerically to accommodate that $v_{\text{PV1}}(i_{\text{PV1}})$ has a nonlinear relationship with the current passing through the PV, i.e., $i_{\text{PV}} = i_{\text{circ}} + i_{\text{out}}$. In the equation presented, $r_{\text{eq}} = 2r_{\text{DS(on)}} + r_{\text{PV(s)}_j} + r_{\text{bt}_{(j+1)}}$ represents the equivalent resistance in the current path for the jth module interconnection. This resistance includes the drain–source resistance of the transistor ($r_{\text{DS(on)}}$), the resistance of PV ($r_{\text{PV(s)}_j}$), and the resistance of the battery ($r_{\text{bt}_{(j+1)}}$).

As the maximum power of the PV is not known and its voltage has a nonlinear relationship with its current due to factors such as temperature and irradiance changes, solving the required duration of T_{b} compared to T_{p} is not trivial. The relationship between v_{PV} and i_{PV} under varying conditions, such as temperature and irradiance, can be represented by [61]

$$i_{\text{PV}} = i_{\text{ph}} - i_0 \left(e^{q\left(\frac{v_{\text{PV}} + r_{\text{PV(s)}} i_{\text{PV}}}{n v_{\text{T}}}\right)} - 1 \right) - \left(\frac{v_{\text{PV}} + r_{\text{PV(s)}} i_{\text{PV}}}{r_{\text{sh}}} \right) \tag{14}$$

where i_{ph} is the photocurrent (current generated by incident light), i_0 the reverse saturation current (diode saturation current), q the elementary charge (electron charge), v_T the thermal voltage (a constant value related to the temperature of the PV module and Boltzmann's constant), n the diode factor (indicating how closely the diode in the PV module behaves like an ideal diode), $r_{\text{PV(s)}}$ the series resistance, and r_{sh} is the shunt resistance.

We simplified the $i_{\text{PV}} - v_{\text{PV}}$ equation as follows: 1) the exponential term in (14) can be linearized for small deviations around the operating point with the first-order Taylor term of the exponential function; 2) irradiance and temperature remain constant; and 3) neglect shunt resistance. Applying the approximation $e^x \approx x + 1$, (14) becomes

$$i_{\text{PV}} \approx i_{\text{ph}} - i_0 \left(\frac{v_{\text{PV}} + r_{\text{PV(s)}} i_{\text{PV}}}{n v_{\text{T}}} \right) - \left(\frac{v_{\text{PV}} + r_{\text{PV(s)}} i_{\text{PV}}}{r_{\text{sh}}} \right). \tag{15}$$

By replacing i_{ph} with i_{G0}, treating v_{T} as a constant, and omitting the term involving r_{sh}

$$i_{\mathrm{PV}} \approx i_{\mathrm{G0}} - i_0 \left(\frac{v_{\mathrm{PV}} + r_{\mathrm{PV(s)}} i_{\mathrm{PV}}}{n v_{\mathrm{T}}} \right) \rightarrow v_{\mathrm{PV}} = f\left(i_{\mathrm{PV}}\right) \approx \left(\frac{n v_{\mathrm{T}} i_{\mathrm{G0}} - i_0 i_{\mathrm{PV}} r_{\mathrm{PV(s)}} - n v_{\mathrm{T}} i_{\mathrm{PV}}}{i_0} \right). \tag{16}$$

When v_{PV1} exceeds that of v_{bt}, i_{circ} flows from PV_1 to the battery during the parallel mode. During the series mode, the integral of the voltage across the inductors, neglecting resistive elements, is zero. In the parallel mode, it becomes $\int v_{\mathrm{L}} \mathrm{d}t = (v_{\mathrm{PV1}} - v_{\mathrm{bt}}) T_{\mathrm{p}}$, and during the boost mode, it turns into $\int v_{\mathrm{L}} \mathrm{d}t = -v_{\mathrm{PV1}} T_{\mathrm{b}}$. Assuming no parasitic or core losses, the average voltage across the inductors over one switching period must be zero to indicate no flux accumulation in the core.

Consequently, by replacing v_{PV1} with $f(i_{\mathrm{PV1}})$, the ratio between T_{p} and T_{b} required for nearly zero energy exchange is as follows:

$$\frac{f\left(i_{\mathrm{PV1}}\right) - v_{\mathrm{bt}}}{f\left(i_{\mathrm{PV1}}\right)} = \frac{T_{\mathrm{b}}}{T_{\mathrm{p}}}. \tag{17}$$

Substituting (12) into (17) results in

$$\frac{f\left(i_{\mathrm{PV1}}\right) - v_{\mathrm{bt}}}{f\left(i_{\mathrm{PV1}}\right)} = \frac{2 m_{\mathrm{d1}}}{\left(1 - m_0 - m_{\mathrm{d1}}\right)}. \tag{18}$$

Therefore, the open-loop value, denoted as m_{d1open} in Fig. 6, which is required to keep the circulating current i_{circ} nearly zero between two modules, depends on the module voltages and the modulation index m_0

$$m_{\mathrm{d1,open}} = \frac{\left(f\left(i_{\mathrm{PV1}}\right) - v_{\mathrm{bt}}\right)\ \left(1 - m_0\right)}{f\left(i_{\mathrm{PV1}}\right) + v_{\mathrm{bt}}}. \tag{19}$$

Likewise, we can establish a relationship for the case when v_{PV1} is less than v_{bt}. However, in this scenario, m_{d1open} would be a negative value, and its magnitude can be determined using (19).

To generate a nonzero $i_{\mathrm{circ,\ SS}}$, we need to account for the term associated with the voltage drop across the equivalent resistance of the path. Consequently, the voltage across the inductors with a nonzero circulating current is given by

$$\int v_{\mathrm{L}} \mathrm{d}t = \begin{cases} \left(v_{\mathrm{PV1}} - v_{\mathrm{bt}} - i_{\mathrm{circ}} r_{\mathrm{eq}}\right) T_{\mathrm{p}}, & \text{parallel state} \\ \left(-v_{\mathrm{PV1}} - i_{\mathrm{circ}} r_{\mathrm{eq}}\right) T_{\mathrm{b}}. & \text{Boost state} \end{cases}. \tag{20}$$

Hence, substitution of (12) into (20) and solving for m_{d1open} results in

$$m_{\mathrm{d1open}} = \frac{\left(f\left(i_{\mathrm{PV1}}\right) - v_{\mathrm{bt}} - i_{\mathrm{circ}} r_{\mathrm{eq}}\right)\ \left(1 - m_0\right)}{f\left(i_{\mathrm{PV1}}\right) + v_{\mathrm{bt}} + i_{\mathrm{circ}} r_{\mathrm{eq}}}. \tag{21}$$

This value acts as a starting point for the MPPT algorithm instances to govern the energy transfer between them with varying voltages between the PV and the battery. Knowing the approximate value of the PV currents at MPPT can help further speed up the convergence by setting i_{circ} in (21) to

$$i_{\mathrm{circ}} = i_{\mathrm{MPPT}} - i_{\mathrm{load}} m_0. \tag{22}$$

Additionally, when we set $i_{\mathrm{circ}} = 0$ in (21), the feed-forward loop strives to minimize any energy exchange between modules. Then any conventional MPPT algorithms can easily determine the exact value of m_d for each PV module. In our case, we have used the typical perturb and observe algorithm as an example of a well-known method. Yet, it can be easily replaced in Fig. 6 with any other state-of-the-art algorithm.

IV. DESIGN CONSIDERATIONS

To validate the performance of the proposed system, it is advisable to design the components for continuous-conduction mode operation. The cross-sectional area (A_p) plays a crucial role in the design of the magnetic cores of the inductors [62]. A_p can be tailored according to the following parameters:

$$A_p = \left[K_i L I^2 \sqrt{1+\gamma} \middle/ B_{\max} K_t \sqrt{K_u \Delta T} \right]^{8/7} \tag{23}$$

where K_u represents the window utilization factor, K_t signifies the stacking factor (with a constant value of 48 200), γ denotes the ratio of iron losses to copper losses, $B_{\max}$ stands for the maximum flux density, L represents the inductance value, I is the peak current, K_i denotes the current waveform factor, and ΔT indicates the temperature rise. Assuming constant values for γ, $B_{\max}$, ΔT, K_i, and K_u, the cross-sectional area A_p is directly proportional to $I^{16/7}$, a factor equal to the maximum amplitude of i_{circ} in the proposed topology. It is essential to ensure that the inductor does not reach saturation at the peak of i_{circ} during continuous operation. When $v_{\mathrm{PV1}} \geq v_{\mathrm{bt}}$, the magnetizing term of the inductor current ($i_L^{\mathrm{magnetize}}$) follows:

$$i_L^{\mathrm{magnetize}} \leq i_{\mathrm{circ}} \leq i_{\mathrm{circ}}^{\mathrm{rated}} + \frac{2 v_{\mathrm{PV1}} m_{\mathrm{d1}}}{L_{\mathrm{eff,DM}} f_{\mathrm{sw}}} \tag{24}$$

where $i_{\mathrm{circ}}^{\mathrm{rated}}$ represents the rated average circulating current for the interconnections. To control and limit the peak circulating current, the necessary inductor value can be determined by

$$L_{\mathrm{eff,DM}} \geq \frac{2 v_{\mathrm{PV1}}^{\max} m_{\mathrm{d1}}}{\Delta i_{\mathrm{diff}} f_{\mathrm{sw}}}. \tag{25}$$

We consider $i_{\mathrm{diff}} = i_{\mathrm{out}}^{\mathrm{rated}} - i_{\mathrm{circ}}^{\mathrm{rated}}$ to be the maximum allowable inductor current ripple. The inductor L_{filter} is an essential component as it forms a low-pass LC filter in conjunction with C_{out}. To maintain a maximum output current ripple of 5%, we can calculate the minimum necessary inductance per

$$L_{\mathrm{filter}} \geq \frac{v_{\mathrm{out}}\left(m_0\right)}{0.05 i_{\mathrm{out}}^{\mathrm{rated}} N f_{\mathrm{sw}}}. \tag{26}$$

Disregarding the equivalent series resistance and permitting a 1% voltage ripple for the capacitor, C_{out} is determined in consideration of the maximum allowed voltage ripple ($\Delta v_{\mathrm{out}} \leq 0.01 V_{\mathrm{out}}$)

$$C_{\mathrm{out}} = \frac{v_{\mathrm{out}} D}{R_{\mathrm{out}} \Delta v_{\mathrm{out}} f_{\mathrm{sw}}}. \tag{27}$$

V. SIMULATION STUDY

To assess the compatibility of the PV and battery system with control requirements, we developed a simulation model in the MATLAB/Simulink software. Table I provides the parameters

TABLE I
SYSTEM AND CONTROL PARAMETERS

Parameters	Description	Sim.	Exp.
P_{1max}	Maximum output power of PV_1 at irradiance = 1000 W/m^2	20.46 kW	14.6 kW
P_{2max}	Maximum output power of PV_2 at irradiance = 1000 W/m^2	20.46 kW	17.8 kW
v_1	Voltage of PV_1 array at irradiance = 1000W/m^2	348 V	348 V
v_2	Voltage of PV_2 array at irradiance = 1000 W/m^2	350 V	350 V
SOC	Initial state-of-charge	80 %	80 %
R_{out}	Load resistance	5 Ω	(10,40) Ω
f_{sw}	Carrier frequency of DC/DC circuit	10 kHz	10 kHz
M_{12}, M_{21}	Mutual inductance of the coupled inductor	24 µH	24 µH
C_{out}	Output capacitance	600 µF	600 µF
L_{filter}	DC inductance	0.8 mH	0.8 mH
L_1, L_2	Self-inductance of the coupled inductor	25 µH	25 µH

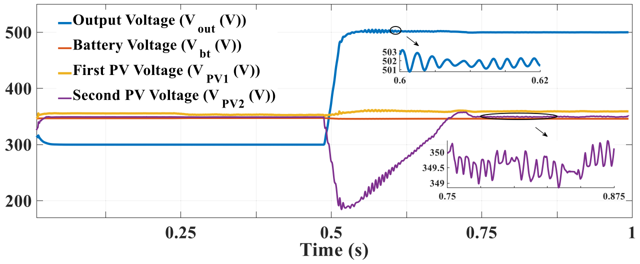

Fig. 7. Simulation results of v_{out}, v_{bt}, v_{PV1}, and v_{PV2}.

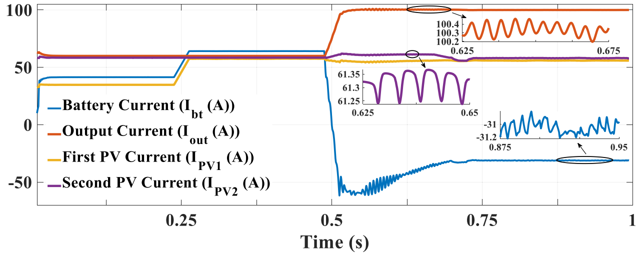

Fig. 8. Simulation results of i_{out}, i_{bt}, i_{PV1}, and i_{PV2}.

for PVs, battery, load, and coupled inductors. Contrary to state-of-the-art modular PV systems, two PV modules and one battery module can generate one additional voltage level, i.e., four levels as opposed to three levels.

Figs. 7 and 8 illustrate the ability of the system to follow v_{out} while operating the PVs at MPPT. The irradiance of PV_1 (E_{PV1}) changes from 600 W/m^2 to 1000 W/m^2 at approximately $t = 0.22$ s and v_{out} from 300 V to 500 V at $t = 0.47$ s. Fig. 7 presents v_{out} as well as the modules' voltages and demonstrates that the system can readily follow the reference voltage ($v_{\mathrm{out\text{-}ref}}$) with a steady state voltage ripple of less than 1%. Additionally, Fig. 8 depicts the current waveforms that depict a small current ripple at the output of the system.

At the interval of 0.2 s to 0.25 s, there is a discernible correlation between the rise in radiation levels and the increased output power from PV_1, generating a total output power exceeding the load power leading to a corresponding increase of the battery charging current. Consequently, the battery charging current increases from approximately 40 A to above 60 A. Notably, during the period from 0.25 to 0.5 s, v_{out} remains constant, and no disturbances are observed at the output voltage. Up to this point, the load is exclusively sustained by the PVs, and excess energy is transferred to the battery. Furthermore, the voltages of both the battery and PVs are in equilibrium (see Fig. 7).

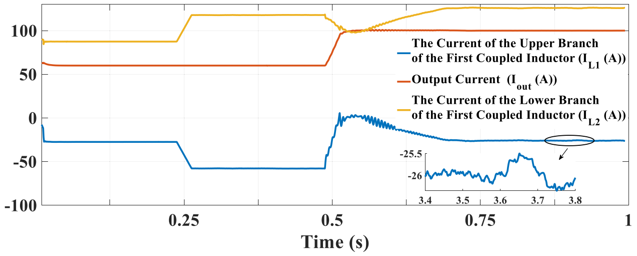

Fig. 9. Simulation results of i_{L1}, i_{L2}, and i_{out}.

By adjusting $v_{\mathrm{out\text{-}ref}}$ to 500 V, the output power is doubled, and the PVs' powers become insufficient to supply the load completely. Therefore, at the new operating point of the system, the battery and PVs collaboratively work towards supplying the load. After such a drastic change in the output power, there are some transients while the MPPT algorithms regulate the energy exchange between the PVs and batteries to ensure that PVs still operate at MPP. Although the MPP of the PVs is obviously not affected by the change in the output load, their operating modulation index (m_0) is. The necessary adjustment of the modulation index requires an update of m_d to maintain the same MPP. Fig. 7 illustrates that approximately 0.13 s are required for panels to reach $> 98\%$ of their MPPs.

Fig. 9 plots the current through the two coils of the first coupled inductor. According to (1), summation of the current of the upper and lower inductor provides i_{out}, emphasizing carefully the design considerations.

In the event of failure in one PV module, the battery and the remaining modules can supply the load. Notably, the control algorithm remains unchanged, adjusting the connection mode between the remaining modules to meet system output voltage and power requirements. The modulation index of the failed module will be set to constant bypass state.

Freewheeling paths are important for maintaining the current flow and ensuring system efficiency during switching transitions. The free-wheeling paths for the coupled inductors form dynamically through the transistors' diodes and are specific to the particular operation.

It is noteworthy that the structure achieves a uniform distribution of the changes in the system's output voltage to the three energy sources regardless of their individual MPPs. The battery module manages all power deficits and surpluses between the PV modules and the output, and can further increase the output voltage if necessary.

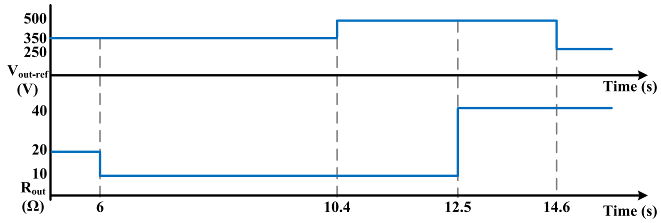

Fig. 10. Dynamic variations of $v_{\mathrm{out\text{-}ref}}$ and R_{out}.

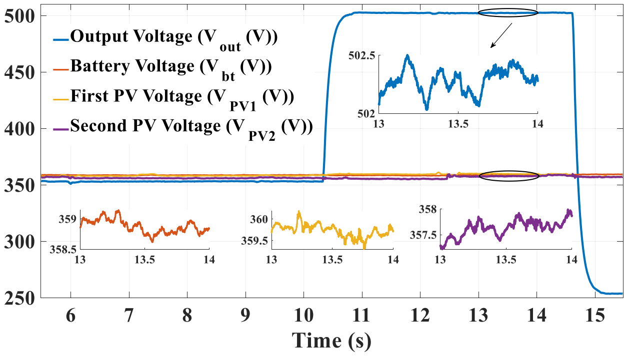

Fig. 11. Experimental results of dynamic v_{out}, v_{bt}, v_{PV1}, and v_{PV2} according to variations of $v_{\mathrm{out\text{-}ref}}$ and R_{out} in Fig. 10.

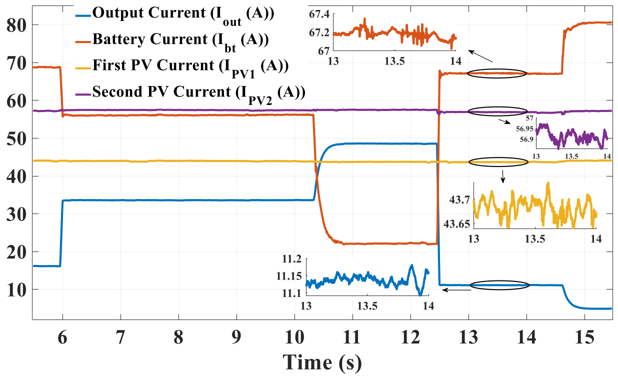

Fig. 12. Experimental results of dynamic i_{out}, i_{bt}, i_{PV1}, and i_{PV2} according to variations of $v_{\mathrm{out\text{-}ref}}$ and R_{out} in Fig. 10.

VI. EXPERIMENTAL STUDY

A. Hardware-in-the-Loop Experiment

For further verification of the system, we perform hardware-in-the-loop experiments with an OPAL-RT system. Experimental tests are divided into two parts. Fig. 10 illustrates the temporal development of the load and $v_{\mathrm{out\text{-}ref}}$ during the first scenario. Before $t = 6$ s, $v_{\mathrm{out\text{-}ref}}$ is set at 350 V, and, as depicted in Fig. 11, v_{out} converges correspondingly and reaches 350 V with a 1.5% voltage ripple. In Fig. 11, v_{bt}, v_{PV1}, and v_{PV2} exhibit an equilibrium. Each of the voltages contributes to the supply of the load. Additionally, Fig. 12 illustrates that the battery starts to charge, reaching approximately 70 A, to absorb the excess energy generated by the PV panels at their MPP. At 6 s, v_{bt}, v_{PV1}, and v_{PV2} remain steady despite an increase in load, indicating voltage equilibrium. Concurrently, with the surge in i_{out} in Fig. 12, i_{PV1}, and i_{PV2} stay constant. Concurrently, the charging current from the battery decreases to about 55 A as the battery charging current is reduced to compensate for the increase in consumed power by the load. At 10.4 s, the PI_1 controller translates an adjustment in $v_{\mathrm{out\text{-}ref}}$ from 350 V to 500 V, which leads to corresponding changes in v_{out} (see Fig. 11). Simultaneously, v_{bt}, v_{PV1}, and v_{PV2} maintain the equilibrium. However, Fig. 12 illustrates that increased v_{out} and consequently doubling load power decreases the battery charging current further. Importantly, i_{bt}, i_{PV1}, and i_{PV2} remain constant, signaling the consistent maintenance of MPPT in both PVs. Following a reduction in the load at 12.5 s while keeping $v_{\mathrm{out\text{-}ref}}$ constant, v_{out} in Fig. 11 remains unchanged and stays stable. However, after 12.5 s, the battery charging current increases, whereas i_{PV1} and i_{PV2} remain constant, which indicates that the system maintains operation at MPP. After 14.6 s, $v_{\mathrm{out\text{-}ref}}$ shifts to 250 V. Although v_{out} promptly converges to this value, v_{bt}, v_{PV1}, and v_{PV2} remain unaltered.

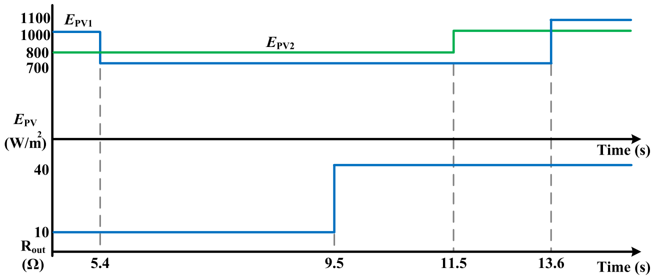

Fig. 13. Dynamic variations of $i_{r,\mathrm{PV}}$ and R_{load}.

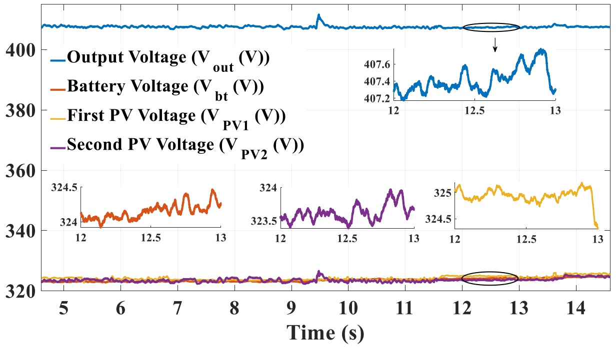

Fig. 14. Experimental results of dynamic v_{out}, v_{bt}, v_{PV1}, and v_{PV2} according to variations of $i_{r,\mathrm{PV}}$ and R_{load} in Fig. 13.

The second scenario studies the MPP operation under varying irradiance (see Fig. 13). During this scenario, $v_{\mathrm{out\text{-}ref}}$ is maintained at 410 V. As Fig. 14 illustrates, v_{out} tracks this value throughout the experiment. At 5.4 s, E_{PV1} decreases from 1000 W/m^2 to 700 W/m^2. Despite this change, v_{bt}, v_{PV1}, and v_{PV2} remain nearly unchanged with no noticeable changes as PV1 reaches its new MPP. Fig. 15 corroborates that i_{PV2} remains constant. However, i_{PV1} decreases, which consequently results in the charging current of the battery (i_{bt}) to also decrease from approximately 45 A to 30 A. At 9.5 s, R_{out} is increased to

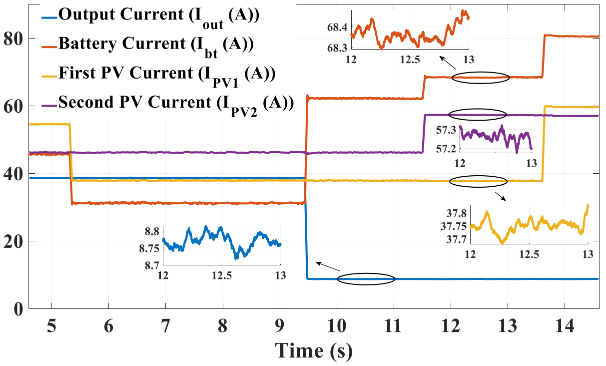

Fig. 15. Experimental results of dynamic i_{out}, i_{bt}, i_{PV1}, and i_{PV2} according to variations of $i_{r,\mathrm{PV}}$ and R_{load} in Fig. 13.

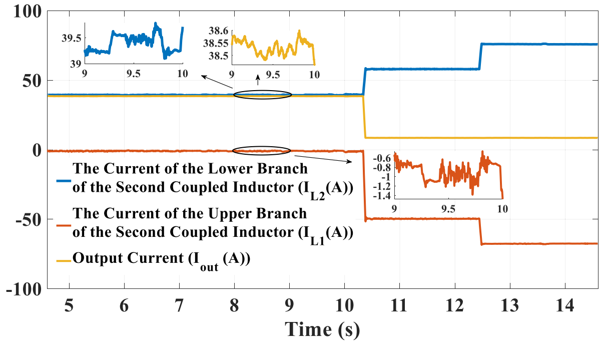

Fig. 16. Experimental results of dynamic i_{L1}, i_{L2}, and i_{out} according to variations of $i_{r,\mathrm{PV}}$ and R_{load} in Fig. 13.

40 Ω, reducing the load by a factor of four. As depicted in Fig. 14, v_{bt}, v_{PV1}, and v_{PV2} remain stable. There is a small momentary transient (less than 3%) in the output voltage due to the significant change in the load, but after the initial disturbance, the voltage control loop brings the output voltage back to its reference value. In Fig. 15, i_{bt} increases significantly due to the decreased R_{out} as the MPPT instances channel the excess energy of the PV panels to the battery. By 11.5 s, E_{PV2} shifts from 800 W/m^2 to 1000 W/m^2. Fig. 15 illustrates an increase in i_{PV2} from about 45 A to approximately 58 A, accompanied by a rise in battery charging current. At 13.6 s, E_{PV1} increases to 1100 W/m^2 and raises i_{PV1} as well as the battery's current.

Upon examining Figs. 7, 11, and 14, it is clear that the voltages of the PV elements and batteries are nearly identical. Although the voltage across the switches when turned OFF varies with different switching modes shown in Figs. 2(a), 3(a), and 4(a), the voltage stress remains symmetric across all components. This uniform stress distribution reduces the likelihood of premature failure due to overvoltage, enhancing system reliability and longevity.

Except when the load is changed, i_{out} and v_{out} remain constant throughout the scenario. This constancy highlights the ability of the system to decouple the output voltage control loop from the MPPT controllers. Fig. 16 illustrates the inherent relationship between i_{circ}, i_{out}, i_{L1}, and i_{L2}. Fig. 16 corroborates the assertion of an evenly distributed output current between the coupled inductors when the inductances are symmetric, as outlined in (1).

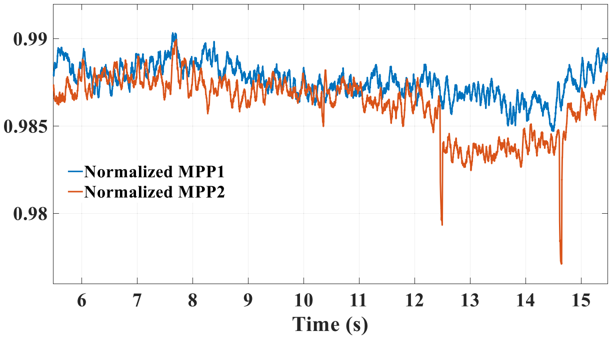

Fig. 17. Normalized MPP (instantaneous power/ $\mathrm{P}_{\max}$) of the PVs.

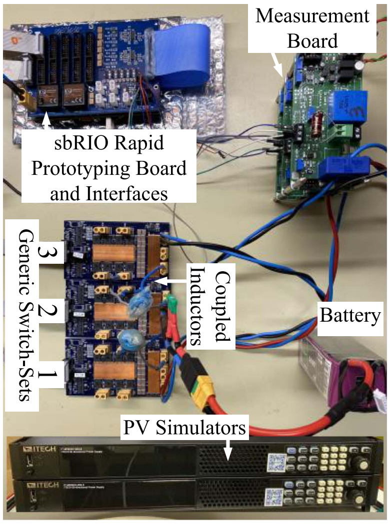

Fig. 18. Test bench of the proposed circuit.

Fig. 17 illustrates the normalized maximum power point values of PV systems. It is evident that the maximum power point values remain consistently above 98% throughout the entire duration. The high MPPT efficiency affirms the effective operation of the controllers. The results demonstrate that the proposed PV–battery system operates every PV element at its MPP. Moreover, when one PV array is working in the shadow and the irradiance of that part is reduced, the system will automatically adjust its corresponding power routing. Meanwhile, the performance of other submodules with better irradiance will not be affected. Such adaptation on the module level through the inductive interconnection improves the overall energy conversion capability of the system.

B. Real-World Experimental Results

Fig. 18 shows the implemented reconfigurable mixed PV-battery system. Table II summarizes the system parameters. Similar to the simulation setup, the experimental setup includes three modules, each with two interconnections equipped with coupled inductors. Each module consists of two half-bridge legs

TABLE II
SYSTEM PARAMETERS IN EXPERIMENTAL TEST

Parameter	Experiment
Carrier frequency for quasi-DC–DC circuits	10 kHz
Number of modules	3
Battery nominal voltage v_{bn}	22 V<v_{b1}<23 V
Coupled inductors	25 µH
$L_{\text{eff,CM}}$	≈ 0 µH
$L_{\text{eff,DM}}$	100 µH
Switch	MOSFET
	r_{DS}: 2 mΩ
	v_{DS}: 100 V
	i_{D}: 300 A
Load resistance	5 Ω
Output power	0.18 – 0.4 kW
Output capacitance	430 µF
DC inductance (L_{filter})	0.33 mH

TABLE III
PV PARAMETERS

Parameter	Experiment
Maximum power	175.1 W
Cells per modules	48
Open circuit voltage v_{oc}	29.29 V
Short circuit current i_{sc}	8.03 A
Voltage at maximum power point v_{mp}	23.41 V
Current at maximum power point i_{mp}	7.48 A

with IPT015N10N5 transistors ($r_{(\text{DS(ON)})} = 2$ mΩ). The dc bus of the second module is connected to a lithium-ion battery with a 6s2p configuration, a nominal voltage of 22.2 V, and a capacity of 5 Ah. The first and third modules are connected to PV simulators with the parameters given in Table III. Additionally, each module features a small array of ceramic capacitors, approximately 300 µF, in parallel with the inputs to provide a low impedance path during the commutation of the switching states.

The voltage and current sensors used in the test bench are commercially available LV 25-P and LA 55-P models from LEM, which provide isolated measurements with a bandwidth of approximately 10 kHz. The controller is implemented on an sbRIO 9627 rapid-control-prototyping board from National Instruments, which features a Zynq-7020 system on chip. This controller receives the output reference voltage ($v_{(\text{out-ref})}$) and the measurements from the sensor boards shown in Fig. 18, and then generates the gate signals according to the control strategy outlined in Fig. 6 of the article.

ITECH bidirectional power supplies, model IT-M3902C-800-8, act as PV simulators. ITECH solar array simulation software, SAS1000M, controlled the devices.

The values of the elements in each inductor can slightly vary due to manufacturing tolerances in winding and core materials. However, the topology accommodates these differences among the coupled inductors while preserving their intended function. The crucial factor is ensuring that the self and mutual inductances within each group of coupled inductors are consistent and equal to avoid mismatching. The measured inductances in each inductor set are $L_1 = M_{12} = M_{21} = L_2 = (25 \pm 1)$ µH, which result in approximately 100 µH differential-mode and nearly zero common-mode inductance. Due to the cancellation effect of the self and mutual inductances of the coupled inductors, the results align precisely with the scenario where all the self and mutual inductances are identical ($L_1 = M_{12} = M_{21} = L_2 =$ 25 µH).

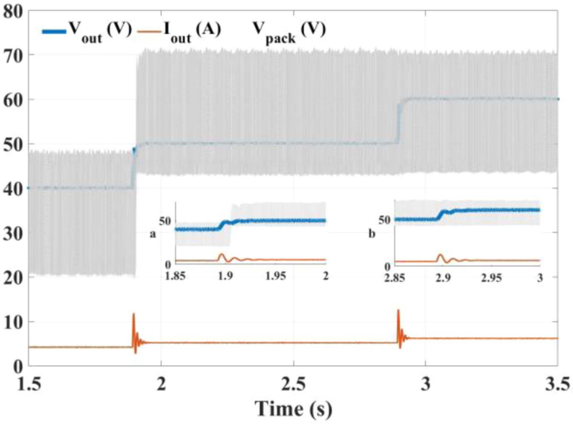

Fig. 19. Experimental results of dynamic v_{out}, v_{pack}, and i_{out}.

The coupled inductor uses a toroidal core (part number B64290L0038X027). If a standard inductor were used instead of a coupled inductor to handle high current in the parallel mode, the required inductance value would be 230 µH with a current rating of 10 A, based on (25), and parameters such as $v_b^{\max} =$ 23 V, $m_{\text{d2}} = 0.05$, $f_{\text{sw}} = 10$ kHz, and $\Delta i_{\text{diff}} = 10\% \times 10$ A. In contrast, inductors based on our proposed solution need to manage only a fraction of the load current, allowing for a significantly smaller core size.

It is important to note that this calculation is simplified, and a comprehensive design should consider additional factors such as core material, saturation current, temperature rise, and efficiency [63].

We examine the system's behavior both in terms of output performance and module interactions. The modules are deliberately unbalanced with a voltage difference of approximately 5%. In conventional systems, this would result in significant circulating currents between the modules.

Fig. 19 demonstrates the proposed system's ability to follow the reference voltage for v_{out}. $v_{(\text{out-ref})}$, is increased in steps from 40 V to 60 V, illustrating the controller's capability to track the reference signal. Fig. 19 shows the output voltage and current profiles, along with the pulsating output voltage of the reconfigurable battery pack (v_{pack}), which operates at an effective switching rate three times the switching frequency of a single module.

Figs. 20 and 21 demonstrate the system's ability to follow v_{out} while operating the PVs at MPPT. E_{PV1} changes from 1000 W/m^2 to 800 W/m^2 at approximately $t = 53$ s, and E_{PV2} changes from 1000 W/m^2 to 800 W/m^2 at approximately $t =$ 73 s. v_{out} changes from 30 V to 40 V at $t = 33$ s.

Fig. 20 graphs v_{out} along with the modules' voltages to indicate that the system accurately tracks $v_{(\text{out-ref})}$ with a steady-state voltage ripple of less than 1%. Fig. 21 illustrates the current

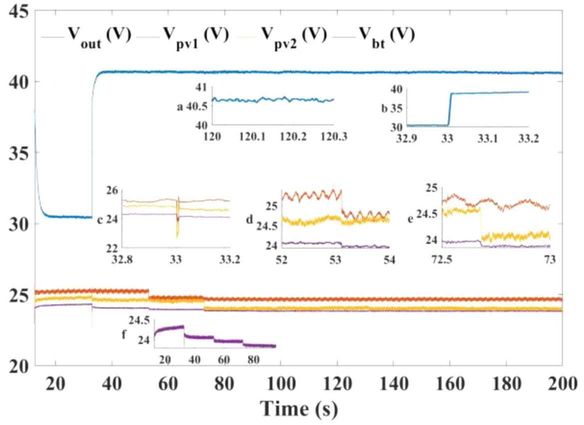

Fig. 20. Real world experimental results of v_{out}, v_{bt}, v_{PV1}, and v_{PV2}.

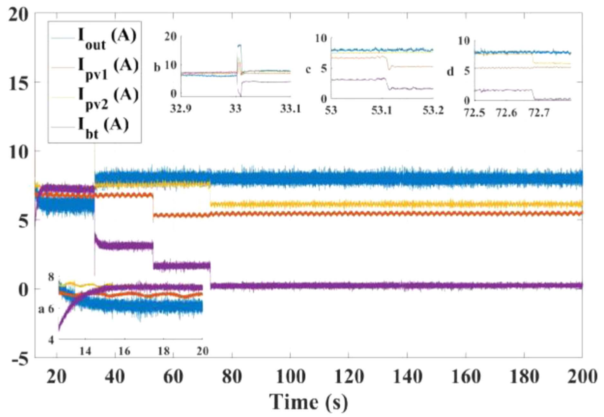

Fig. 21. Real world experimental results of i_{out}, i_{bt}, i_{PV1}, and i_{PV2}.

waveforms and reveals a small current ripple at the system's output. From 53 s onwards, there is a clear correlation between the decrease in irradiance levels and the reduced output power from PV1 and PV2, which results in a total output power that lags behind the load power. This leads to a corresponding decrease in the battery charging current, which drops from approximately 8 A to just above 0 A. Notably, from 33 s onwards, v_{out} remains constant, with no disturbances observed in the output voltage. Before 33 s, the load is exclusively supported by the PVs, and any excess energy is transferred to the battery, maintaining equilibrium in the voltages of both the battery and PVs (see Fig. 20).

Adjusting $v_{(\mathrm{out\text{-}ref})}$ to 40 V enhances the output power, causing the PVs' power to become insufficient to fully supply the load. At this new operating point, the battery charging rate is decreased. This change in output power induces transients, as shown in Fig. 20(a), (b), (c), and (d), while the MPPT algorithms regulate the energy exchange between the PVs and batteries, ensuring the PVs continue to operate at MPP. Although the PV elements MPP is not affected by the change in output load, their operating modulation index (m_0) is. Adjusting the modulation index requires updating m_{d} to maintain the same MPP. Fig. 20

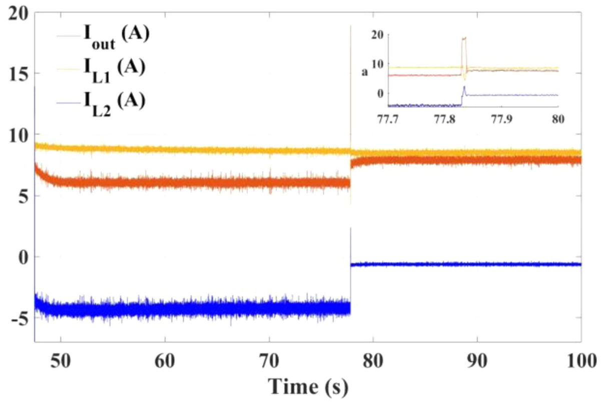

Fig. 22. Real world experimental results of dynamic i_{out}, i_{L1}, and i_{L2}.

illustrates that approximately 0.01 s is needed for the panels to reach over 98% of their MPPs.

Fig. 22 plots the current through the two coils of the first coupled inductor. According to (1), the sum of the currents in the upper and lower inductor provides i_{out}, which emphasizes the importance of careful design considerations.

VII. COMPARISON WITH STATE OF THE ART

Table IV provides a comparative analysis of the attributes of the presented circuit in contrast to recent advancements in the field. There are numerous advantages over other works including the following.

1) The proposed system allows for direct energy exchange between PV modules as well as batteries and eliminates the need for multiple energy conversion stages alternative technologies would need. The omission of multiple conversion stages reduces conversion losses and enhances overall system efficiency.
2) Mutual inductances and a corresponding modulation technique achieve maximum power on the module level and offer increased flexibility in energy transfer as well as load sharing among modules. This flexibility allows for efficient adaptation to varying environmental conditions and load demands.
3) The decoupled control of output voltage and energy exchange (MPPT controllers) rate enables independent optimization of these parameters, leading to improved system performance and efficiency compared to systems with tightly coupled control schemes. The system ensures that each PV module operates at its optimal MPP, maximizing power generation, even under partial shading, and overall system efficiency. Fig. 23 compares the power generation of the presented topology with a system utilizing two cascaded PVs. In the latter system, $E_{\mathrm{PV1(cascaded)}}$ and $E_{\mathrm{PV2(cascaded)}}$, respectively, receive 1000 W/m^2 and 600 W/m^2 radiation. Typically, each PV in the traditional setup may not consistently operate at its MPP simultaneously. However, our presented topology ensures that all PVs operate at their MPP at all times. This results in

TABLE IV
COMPARISON OF PRIOR APPROACHES

Characteristic	[64]	[65]	[66]	[67]	[27]	[68]	[69]	[11]	[70]	Presented work
Energy exchange	no	no	no	no	no	no	no	no	no	yes
Load sharing	no	yes	no	no	no	no	yes	no	no	yes
Independent control	no	no	no	no	no	no	no	no	no	yes
Modules balancing	yes	yes	yes	no	no	yes	yes	no	no	yes
Optimized MPPT	complex	no	complex	no	complex	simple	simple	complex	simple	simple
Reliability	low	low	low	high	high	low	high	low	high	high

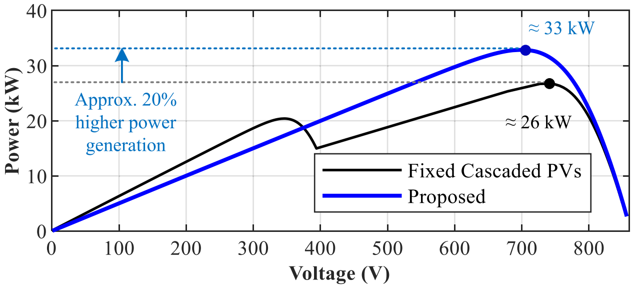

Fig. 23. Comparison of the power generation of the presented topology with a system utilizing two cascaded PVs.

a notable enhancement of approximately 19% in energy yield compared to the conventional state.

4) The ability of battery modules to contribute to output voltage granulation reduces the output voltage dependability to the PV panels, particularly in scenarios with fluctuating energy generation, and concurrently allows for generating additional voltage levels.
5) The design of mutual inductors with minimal common-mode inductance reduces energy losses and improves system efficiency. This design feature sets the system apart from others by optimizing energy transfer efficiency.

In previous circuits, both the PV and battery require a dc–dc converter to connect to the dc bus outside of the modules, which increases the cost [64], [70]. Alternatively, the PV panel can feed through a dc–dc boost converter, while a battery is connected to the module dc bus via a bidirectional dc–dc boost converter, which includes two switches, a capacitor, and an inductor [65]. Other circuits directly connect the mixed PV-battery system to the ac grid via a full bridge converter, but they lack provisions for energy exchange, load sharing, module balancing, and reliability in the system [66], [67], [27], [68], [69], [11], [70].

It is sufficient to replace the half bridge in each group with a full bridge to generate an ac voltage at the terminal of the modular reconfigurable system and subsequently connect the proposed system to the grid. Conversely, each individual battery and PV module is connected to a full bridge [64], [65], [67], [27], [68], [69], [70]. Therefore, from the perspectives of complexity, cost and the number of semiconductors, the proposed topology has significant advantages. Additionally, Wang et al. [11] and Liu et al. [66] proposed a topology of the dual-dc-port dc–ac converter, which incorporates a diode to prevent a system short circuit in the absence of sunlight.

Contrary to other works, the modular design allows for easy scalability by adding or removing PV and battery modules without significant changes to the overall system architecture. This flexibility is particularly advantageous for expanding or downsizing installations to meet changing energy demands. Moreover, the design minimizes the number of required dc–dc converters to reduce initial setup costs and maintenance expenses. The fewer energy conversion stages lower losses and lead to higher overall efficiency as well as lower operational costs. The system maintains optimal performance under various operating conditions, including temperature extremes, weather fluctuations, and grid disturbances. The ability to ensure each PV module operates at its maximum power point even under partial shading significantly enhances overall system efficiency and reliability. Besides, the flexible, and modular architecture facilitates integration with existing grid networks, reducing implementation challenges and costs. Plus, the ability to decouple control of output voltage and energy exchange rates further enhances system stability and performance.

We also compared various module-based topologies with respect to component count and efficiency. Although the proposed topology uses a higher number of individual transistors compared to the literature [71], [72], [73], [74], [75], [76], [77], these additional transistors increase the output rating by the same level. Furthermore, the system demonstrates advantages in the count of capacitors, inductors, and diodes. The increased number of transistors in our topology directly contributes to enhanced functionality and flexibility. Each transistor serves multiple roles and enables dynamic mode switching (series, parallel, and boost) and efficient energy management between PV modules and batteries. While a higher component count might seem to imply reduced reliability, our design leverages this count to provide redundancy. The system can maintain operation even if some components fail, thereby enhancing overall reliability. Moreover, the integration of multiple operational modes and advanced energy transfer techniques, facilitated by the higher transistor count, results in significant efficiency gains. This efficiency can lead to lower thermal stress and improved longevity of the system components.

Table V provides a quantitative comparison between our proposed topology and the literature [71], [72], [73], [74], [75], [76], [77]. Although some circuits from the literature exhibit high efficiency and lower transistor counts, they often lack in energy transfer between modules and load sharing, which can reduce overall system efficiency. Additionally, our proposed circuit's

TABLE V
COMPARISON OF MODULE-BASED APPROACHES

Attribute	[71]	[72]	[73]	[74]	[75]	[76]	[77]	Presented work
Number of Transistors in each module	1	2	2	2	2	2	2	4
Number of Diodes in each module	4	0	3	2	2	0	0	0
Number of Inductors in each module	1	1	4	2	1	1	1	1
Number of Capacitors in each module	5	2	3	2	4	2	2	0
System Efficiency (%)	96.7	99	92	98.2	92.7	99	90.23	98
Energy exchange	no	no	no	no	no	no	no	yes
Load sharing	no	no	no	no	no	no	no	yes

modularity allows us to generate an ac output by substituting half-bridges in modules with full bridges, a feature not possible with other works apart from few exceptions [75].

VIII. CONCLUSION

This article introduced a novel reconfigurable PV–battery hybrid system that enhances energy utilization and flexibility. The proposed architecture employs modular reconfigurable circuits with compact coupled inductors and an innovative modulation strategy to ensure each PV module operates at its MPP. This design mitigates the limitations of traditional rigid connections, such as local optima and scalability issues.

Key advantages of our system include the following.

1) Efficient bidirectional energy transfer between PV modules and batteries, which reduces the need for multiple energy conversion stages and minimizes conversion losses.
2) Enhanced load sharing and module balancing, facilitated by coupled inductors, which offer minimal common-mode inductance and high differential-mode inductance.
3) Decoupled control of output voltage and energy exchange rates, which allow independent optimization and improved system performance.

Simulation, hardware-in-the-loop test, and experimental analysis validated the system's performance and demonstrated at least 97% MPP tracking efficiency, approximately 19% increase in energy output compared to conventional setups, and less than 1% ripple in voltage and current. These results underscore the system's capability to maintain stable and reliable operation under varying conditions. The proposed topology's benefits are especially pronounced in higher power scenarios. They suggest it as a promising solution for advancing renewable energy systems and direct dc–ac conversion.

REFERENCES

[1] J. Joshi, "Do renewable portfolio standards increase renewable energy capacity? Evidence from the United States," *J. Environ. Manage.*, vol. 287, 2021, Art. no. 112261.

[2] B. Buchner et al., "Global landscape of climate finance 2015," *Climate Policy Initiative*, vol. 32, pp. 1–38, 2014.

[3] A. I. Elsanabary, G. Konstantinou, S. Mekhilef, C. D. Townsend, M. Seyedmahmoudian, and A. Stojcevski, "Medium voltage large-scale grid-connected photovoltaic systems using cascaded H-bridge and modular multilevel converters: A review," *IEEE Access*, vol. 8, pp. 223686–223699, 2020.

[4] R. Selvamuthukumaran, A. Garg, and R. Gupta, "Hybrid multicarrier modulation to reduce leakage current in a transformerless cascaded multilevel inverter for photovoltaic systems," *IEEE Trans. Power Electron.*, vol. 30, no. 4, pp. 1779–1783, Apr. 2015.

[5] F. M. Alhuwaishel, A. K. Allehyani, S. A. S. Al-Obaidi, and P. N. Enjeti, "A medium-voltage DC-collection grid for large-scale PV power plants with interleaved modular multilevel converter," *IEEE J. Emerg. Sel. Topics Power Electron.*, vol. 8, no. 4, pp. 3434–3443, Dec. 2020.

[6] Z. Huang, D. Zhou, L. Wang, Z. Shen, and Y. Li, "A review of single-stage multiport inverters for multisource applications," *IEEE Trans. Power Electron.*, vol. 38, no. 5, pp. 6566–6584, May 2023.

[7] T. S. Basu, S. Maiti, and C. Chakraborty, "Performance improvement of PV-fed hybrid modular multilevel converter under partial shading condition," *IEEE Trans. Ind. Electron.*, vol. 68, no. 10, pp. 9652–9664, Oct. 2021.

[8] S. Nayak, A. Das, R. E. Torres-Olguin, S. D'Arco, and G. Guidi, "Battery energy support to cascaded H-bridge converter-fed large-scale PV system during unbalanced power generation," *IEEE Trans. Ind. Appl.*, vol. 58, no. 6, pp. 7479–7489, Nov./Dec. 2022.

[9] M. Rouholamini et al., "A review of modeling, management, and applications of grid-connected li-ion battery storage systems," *IEEE Trans. Smart Grid*, vol. 13, no. 6, pp. 4505–4524, Nov. 2022.

[10] S. Nayak and A. Das, "A DAB based folder-unfolder circuit in cascaded H-bridge converter for MV grid application," in *Proc. IEEE Int. Conf. Power Electron., Drives Energy Syst.*, Jaipur, India, 2022, pp. 1–6.

[11] J. Wang, K. Sun, D. Zhou, and Y. Li, "Virtual SVPWM-based flexible power control for dual-dc-port DC–AC converters in PV–battery hybrid systems," *IEEE Trans. Power Electron.*, vol. 36, no. 10, pp. 11431–11443, Oct. 2021.

[12] Z. Wang, Q. Luo, Y. Wei, D. Mou, X. Lu, and P. Sun, "Topology analysis and review of three-port DC–DC converters," *IEEE Trans. Power Electron.*, vol. 35, no. 11, pp. 11783–11800, Nov. 2020.

[13] V. Jayan and A. M. Y. M. Ghias, "A single-objective modulated model predictive control for a multilevel flying-capacitor converter in a DC microgrid," *IEEE Trans. Power Electron.*, vol. 37, no. 2, pp. 1560–1569, Feb. 2022.

[14] A. Kumar and V. Verma, "Performance enhancement of single-phase grid-connected PV system under partial shading using cascaded multilevel converter," *IEEE Trans. Ind. Appl.*, vol. 54, no. 3, pp. 2665–2676, May/Jun. 2018.

[15] P. R. Bana, K. P. Panda, R. T. Naayagi, P. Siano, and G. Panda, "Recently developed reduced switch multilevel inverter for renewable energy integration and drives application: Topologies, comprehensive analysis and comparative evaluation," *IEEE Access*, vol. 7, pp. 54888–54909, 2019.

[16] Z. Zhang et al., "Droop control of a bipolar dc microgrid for load sharing and voltage balancing," in *Proc. IEEE 3rd Int. Future Energy Electro. Conf. ECCE Asia*, Kaohsiung, Taiwan, 2017, pp. 795–799.

[17] D. Yousri, T. S. Babu, E. Beshr, M. B. Eteiba, and D. Allam, "A robust strategy based on marine predators algorithm for large scale photovoltaic array reconfiguration to mitigate the partial shading effect on the performance of PV system," *IEEE Access*, vol. 8, pp. 112407–112426, 2020.

[18] M. Nasir and M. F. Zia, "Global maximum power point tracking algorithm for photovoltaic systems under partial shading conditions," in *Proc. 16th Int. Power Electron. Motion Control Conf. Expo.*, Antalya, Turkey, 2014, pp. 667–672.

[19] B. Su, H. Chen, K. Liu, and W. Liu, "RCAG-net: Residual channelwise attention gate network for hot spot defect detection of photovoltaic farms," *IEEE Trans. Instrum. Meas.*, vol. 2, Jan. 2021, Art. no. 3510514. [Online]. Available: https://www.proceedings.com/24483.html

[20] S. M. Goetz, C. Wang, Z. Li, D. L. Murphy, and A. V. Peterchev, "Concept of a distributed photovoltaic multilevel inverter with cascaded double H-bridge topology," *Int. J. Elect. Power Energy Syst.*, vol. 110, pp. 667–678, 2019.

[21] C. Wang, Z. Li, D. L. K. Murphy, Z. Li, A. V. Peterchev, and S. M. Goetz, "Photovoltaic multilevel inverter with distributed maximum power point tracking and dynamic circuit reconfiguration," in *Proc. IEEE 3rd Int. Future Energy Electron. Conf. ECCE Asia*, Kaohsiung, Taiwan, 2017, pp. 1520–1525.

[22] J. Häring, M. Hepp, W. Wondrak, and M.-M. Bakran, "A neutral point balancing and voltage error compensation approach for fault-tolerant 3-level inverters," *IEEE Open J. Power Electron.*, vol. 5, pp. 106–122, Oct. 2024. [Online]. Available: https://www.proceedings.com/35313.html

[23] R. Phukan, S.-Y. Chen, and R. Burgos, “A systematic methodology for parasitic capacitance estimation and validation of multichip modules,” *IEEE Trans. Ind. Electron.*, vol. 71, no. 3, pp. 2489–2497, Mar. 2024.

[24] A. A. De Melo Bento and L. C. G. S. Garcia, “A comparative study of two high step-up DC-DC voltage converters,” in *Proc. 15th IEEE Int. Conf. Ind. Appl.*, 2023, pp. 407–414.

[25] W. A. P. Castiblanco, A. Toebe, and C. Rech, “Five-level switched-capacitor unidirectional rectifier with reduced number of components,” *IEEE Trans. Power Electron.*, vol. 38, no. 12, pp. 15045–15054, Dec. 2023.

[26] E. Villanueva, P. Correa, J. Rodriguez, and M. Pacas, “Control of a single-phase cascaded H-bridge multilevel inverter for grid-connected photovoltaic systems,” *IEEE Trans. Ind. Electron.*, vol. 56, no. 11, pp. 4399–4406, Nov. 2009.

[27] Q. Zhang and K. Sun, “A flexible power control for PV-battery hybrid system using cascaded H-bridge converters,” *IEEE J. Emerg. Sel. Topics Power Electron.*, vol. 7, no. 4, pp. 2184–2195, Dec. 2019.

[28] M. Quraan, T. Yeo, and P. Tricoli, “Design and control of modular multilevel converters for battery electric vehicles,” *IEEE Trans. Power Electron.*, vol. 31, no. 1, pp. 507–517, Jan. 2016.

[29] N. Katzenburg, K. Kuhlmann, L. Leister, L. Stefanski, J. Teigelkötter, and M. Hiller, “Design of a modular multilevel converter with 400 kWh of integrated batteries,” in *Proc. 22nd Int. Symp. Power Electron.*, 2023, vol. 1, pp. 1–8.

[30] A. Nami, J. Liang, F. Dijkhuizen, and G. D. Demetriades, “Modular multilevel converters for HVDC applications: Review on converter cells and functionalities,” *IEEE Trans. Power Electron.*, vol. 30, no. 1, pp. 18–36, Jan. 2015.

[31] J. Zhang, Y. Zhang, F. Deng, and Z. Din, “Overmodulation operation of hybrid modular multilevel converter with reduced energy storage requirement,” *IEEE J. Emerg. Sel. Topics Power Electron.*, vol. 10, no. 3, pp. 2946–2958, Jun. 2022.

[32] J. Fang, F. Blaabjerg, S. Liu, and S. M. Goetz, “A review of multilevel converters with parallel connectivity,” *IEEE Trans. Power Electron.*, vol. 36, no. 11, pp. 12468–12489, Nov. 2021.

[33] S. M. Goetz, A. V. Peterchev, and T. Weyh, “Modular multilevel converter with series and parallel module connectivity: Topology and control,” *IEEE Trans. Power Electron.*, vol. 30, no. 1, pp. 203–215, Jan. 2015.

[34] J. Fang, Z. Li, and S. M. Goetz, “Multilevel converters with symmetrical half-bridge submodules and sensorless voltage balance,” *IEEE Trans. Power Electron.*, vol. 36, no. 1, pp. 447–458, Jan. 2021.

[35] N. Tashakor, F. Iraji, and S. M. Goetz, “Low-frequency scheduler for optimal conduction loss in series/parallel modular multilevel converters,” *IEEE Trans. Power Electron.*, vol. 37, no. 3, pp. 2551–2561, Mar. 2022.

[36] N. Tashakor, Z. Li, and S. M. Goetz, “A generic scheduling algorithm for low-frequency switching in modular multilevel converters with parallel functionality,” *IEEE Trans. Power Electron.*, vol. 36, no. 3, pp. 2852–2863, Mar. 2021.

[37] Z. Li, R. Lizana F., Z. Yu, S. Sha, A. V. Peterchev, and S. M. Goetz, “A modular multilevel series/parallel converter for a wide frequency range operation,” *IEEE Trans. Power Electron.*, vol. 34, no. 10, pp. 9854–9865, Oct. 2019.

[38] Z. Li, J. K. Motwani, Z. Zeng, S. M. Lukic, A. V. Peterchev, and S. M. Goetz, “A reduced series/parallel module for cascade multilevel static compensators supporting sensorless balancing,” *IEEE Trans. Ind. Electron.*, vol. 68, no. 1, pp. 15–24, Jan. 2021.

[39] S. M. Goetz, Z. Li, X. Liang, C. Zhang, S. M. Lukic, and A. V. Peterchev, “Control of modular multilevel converter with parallel connectivity—Application to battery systems,” *IEEE Trans. Power Electron.*, vol. 32, no. 11, pp. 8381–8392, Nov. 2017.

[40] Z. Li, R. Lizana, Z. Yu, S. Sha, A. V. Peterchev, and S. M. Goetz, “Modulation and control of series/parallel module for ripple-current reduction in star-configured split-battery applications,” *IEEE Trans. Power Electron.*, vol. 35, no. 12, pp. 12977–12987, Dec. 2020.

[41] Z. Li, R. Lizana F., S. Sha, Z. Yu, A. V. Peterchev, and S. M. Goetz, “Module implementation and modulation strategy for sensorless balancing in modular multilevel converters,” *IEEE Trans. Power Electron.*, vol. 34, no. 9, pp. 8405–8416, Sep. 2019.

[42] Z. Li, R. Lizana, A. V. Peterchev, and S. M. Goetz, “Distributed balancing control for modular multilevel series/parallel converter with capability of sensorless operation,” in *Proc. IEEE Energy Convers. Congr. Expo.*, Cincinnati, OH, USA, 2017, pp. 1787–1793.

[43] R. L. F., S. Rivera, Z. Li, J. Luo, A. V. Peterchev, and S. M. Goetz, “Modular multilevel series/parallel converter with switched-inductor energy transfer between modules,” *IEEE Trans. Power Electron.*, vol. 34, no. 5, pp. 4844–4852, May 2019.

[44] S. A. Ibrahim, A. Nasr, and M. A. Enany, “Maximum power point tracking using ANFIS for a reconfigurable PV-based battery charger under non-uniform operating conditions,” *IEEE Access*, vol. 9, pp. 114457–114467, 2021.

[45] H. M. El-Helw, A. Magdy, and M. I. Marei, “A hybrid maximum power point tracking technique for partially shaded photovoltaic arrays,” *IEEE Access*, vol. 5, pp. 11900–11908, 2017.

[46] A. F. Murtaza, H. A. Sher, K. Al-Haddad, and F. Spertino, “Module level electronic circuit based PV array for identification and reconfiguration of bypass modules,” *IEEE Trans. Energy Convers.*, vol. 36, no. 1, pp. 380–389, Mar. 2021.

[47] A. Ramyar and A.-T. Avestruz, “Reconfigurable photovoltaic emulator for differential diffusion charge redistribution solar modules,” *IEEE Trans. Energy Convers.*, vol. 2, pp. 36–46, 2021.

[48] S. Debnath et al., “Renewable integration in hybrid AC/DC systems using a multi-port autonomous reconfigurable solar power plant (MARS),” *IEEE Trans. Power Syst.*, vol. 36, no. 1, pp. 603–612, Jan. 2021.

[49] M. Meraj, S. Rahman, A. Iqbal, and L. Ben-Brahim, “Common mode voltage reduction in a single-phase quasi Z-source inverter for transformerless grid-connected solar PV applications,” *IEEE J. Emerg. Sel. Topics Power Electron.*, vol. 7, no. 2, pp. 1352–1363, Jun. 2019.

[50] A. Mellit, G. M. Tina, and S. A. Kalogirou, “Fault detection and diagnosis methods for photovoltaic systems: A review,” *Renewable Sustain. Energy Rev.*, vol. 91, pp. 1–17, 2018.

[51] H. Qamar, H. Qamar, N. Korada, and R. Ayyanar, “240°-clamped PWM applied to transformerless grid connected PV converters with reduced common mode voltage and superior performance metrics,” *IEEE Open J. Power Electron.*, vol. 3, pp. 153–167, 2022.

[52] M. Schroeder and J. Jaeger, “Advanced energy flow control concept of an MMC for unrestricted operation as a multiport device,” *IEEE Trans. Power Electron.*, vol. 34, no. 11, pp. 11496–11512, Nov. 2019.

[53] H. Bayat and A. Yazdani, “A hybrid MMC-based photovoltaic and battery energy storage system,” *IEEE Power Energy Technol. Syst. J.*, vol. 6, no. 1, pp. 32–40, Mar. 2019.

[54] J. Fang, S. Yang, H. Wang, N. Tashakor, and S. Goetz, “Reduction of MMC capacitances through parallelization of symmetrical half-bridge submodules,” *IEEE Trans. Power Electron.*, vol. 36, no. 8, pp. 8907–8918, Aug. 2021.

[55] N. Tashakor, F. Iraji, and S. G. Goetz, “Low-frequency scheduler for optimal conduction loss in series/parallel modular multilevel converters,” *IEEE Trans. Power Electron.*, vol. 37, no. 3, pp. 2551–2561, Mar. 2022.

[56] X. Hu, Y. Zhu, J. Zhang, F. Deng, and Z. Chen, “Unipolar double-star submodule for modular multilevel converter with DC fault blocking capability,” *IEEE Access*, vol. 7, pp. 136094–136105, 2019.

[57] J. Xu, J. Li, J. Zhang, L. Shi, X. Jia, and C. Zhao, “Open-loop voltage balancing algorithm for two-port full-bridge MMC-HVDC system,” *Int. J. Elect. Power Energy Syst.*, vol. 109, pp. 259–268, Jul. 2019.

[58] N. Tashakor, J. Kacetl, J. Fang, Z. Li, and S. Goetz, “Generic dynamically reconfigurable battery with integrated auxiliary output and balancing capability,” *IEEE Trans. Power Electron.*, vol. 38, no. 7, pp. 7933–7944, Jul. 2023.

[59] N. Tashakor, J. Kacetl, D. Keshavarzi, and S. Goetz, “Topology, analysis, and modulation strategy of a fully controlled modular reconfigurable DC battery pack with interconnected output ports for electric vehicles,” *IEEE Trans. Trans. Electrific.*, vol. 10, no. 1, pp. 1180–1193, Mar. 2024.

[60] N. Tashakor, P. Pourhadi, M. Bayati, M. H. Samimi, J. Fang, and S. M. Goetz, “Modular reconfigurable mixed battery system with heterogeneous modules,” *IEEE Trans. Transp. Electrific.*, vol. 10, no. 1, pp. 1180–1193, Mar. 2024.

[61] H. Tian, F. Mancilla-David, K. Ellis, E. Muljadi, and P. Jenkins, “A cell-to-module-to-array detailed model for photovoltaic panels,” *Sol. Energy*, vol. 86, no. 9, pp. 2695–2706, 2012.

[62] P. Pourhadi, M. H. Samimi, A. Marzoughi, V. Samavatian, H. Iman-Eini, and Y. Naghibzadeh, “A highly reliable low-cost single-switch resonant DC–DC converter with high gain and low component count,” *IEEE Trans. Ind. Electron.*, vol. 70, no. 3, pp. 2556–2565, Mar. 2023.

[63] N. Mohan, T. M. Undeland, and W. P. Robbins, *Power Electronics: Converters, Applications, and Design*. Hoboken, NJ, USA: Wiley, 2003.

[64] C. Lupangu, J. J. Justo, and R. C. Bansal, “Model predictive for reactive power scheduling control strategy for PV–battery hybrid system in competitive energy market,” *IEEE Syst. J.*, vol. 14, no. 3, pp. 4071–4078, Sep. 2020.

[65] Y. Karimi, H. Oraee, and J. M. Guerrero, “Decentralized method for load sharing and power management in a hybrid single/three-phase-islanded microgrid consisting of hybrid source PV/battery units,” *IEEE Trans. Power Electron.*, vol. 32, no. 8, pp. 6135–6144, Aug. 2017.

[66] L. Liu, D. Zhou, J. Zou, and W. Wang, "Zero vector regulation-based closed-loop power distribution strategy for dual-DC-port DC-AC converter-connected PV-battery hybrid systems," *IEEE Trans. Power Electron.*, vol. 38, no. 6, pp. 6956–6968, Jun. 2023.

[67] C. D. Rodríguez-Gallegos et al., "A siting and sizing optimization approach for PV–battery–diesel hybrid systems," *IEEE Trans. Ind. Appl.*, vol. 54, no. 3, pp. 2637–2645, May/Jun. 2018.

[68] H. Xue and J. He, "Flexible power control for extending operating range of PV–Battery hybrid cascaded H-bridge converters under unbalanced power conditions," *IEEE Trans. Ind. Electron.*, vol. 70, no. 8, pp. 8118–8128, Aug. 2023.

[69] Y. Pan, A. Sangwongwanich, Y. Yang, and F. Blaabjerg, "Distributed control of islanded series PV-battery-hybrid systems with low communication burden," *IEEE Trans. Power Electron.*, vol. 36, no. 9, pp. 10199–10213, Sep. 2021.

[70] S. Kumar and B. Singh, "Seamless operation and control of single-phase hybrid PV-BES-utility synchronized system," *IEEE Trans. Ind. Appl.*, vol. 55, no. 2, pp. 1072–1082, Mar./Apr. 2019.

[71] S.-M. Chen, T.-J. Liang, and K.-R. Hu, "Design, analysis, and implementation of solar power optimizer for DC distribution system," *IEEE Trans. Power Electron.*, vol. 28, no. 4, pp. 1764–1772, Apr. 2013.

[72] O. Khan, W. Xiao, and H. H. Zeineldin, "Gallium-nitride-based submodule integrated converters for high-efficiency distributed maximum power point tracking PV applications," *IEEE Trans. Ind. Electron.*, vol. 63, no. 2, pp. 966–975, Feb. 2016.

[73] J. C. d. S. de Morais, J. L. d. S. de Morais, and R. Gules, "Photovoltaic AC module based on a Cuk converter with a switched-inductor structure," *IEEE Trans. Ind. Electron.*, vol. 66, no. 5, pp. 3881–3890, May 2019.

[74] M. S. Agamy et al., "An efficient partial power processing DC/DC converter for distributed PV architectures," *IEEE Trans. Power Electron.*, vol. 29, no. 2, pp. 674–686, Feb. 2014.

[75] H. Jeong, S. Park, J.-H. Jung, T. Kim, A.-R. Kim, and K. A. Kim, "Segmented differential power processing converter unit and control algorithm for photovoltaic systems," *IEEE Trans. Power Electron.*, vol. 36, no. 7, pp. 7797–7809, Jul. 2021.

[76] A. Blumenfeld, A. Cervera, and M. M. Peretz, "Enhanced differential power processor for PV systems: Resonant switched-capacitor gyrator converter with local MPPT," *IEEE J. Emerg. Sel. Topics Power Electron.*, vol. 2, no. 4, pp. 883–892, Dec. 2014.

[77] G. Chu, H. Wen, L. Jiang, Y. Hu, and X. Li, "Bidirectional flyback based isolated-port submodule differential power processing optimizer for photovoltaic applications," *Sol. Energy*, vol. 158, pp. 929–940, 2017.

Wei Jiang received the bachelor's degree in electrical engineering and automation and master's degree in power electronics and electric drive from Anhui University of Science and Technology, Huainan, China, in 2004 and 2007, respectively.

He is currently an Associate Professor with the Department of Intelligent Engineering, Bozhou Vocational and Technical College. He was also a Visiting Researcher with the Department of Electrical and Computer Engineering, University of Kaiserslautern-Landau, Kaiserslautern, Germany. His research interests include modular multilevel converters, photovoltaic and energy storage systems, and ac–dc hybrid microgrids.

Nima Tashakor (Member, IEEE) received the B.Sc. degree from Isfahan University, Isfahan, Iran, in 2013, the M.Sc. degree from Shiraz University, Shiraz, Iran, in 2015, both in electrical power engineering, and the Ph.D. degree in power electronics engineering (with distinction) from the Technical University of Kaiserslautern, Kaiserslautern, Germany.

He is currently with Volkswagen on smart development of next generation electric drives. He explores the applications of machine learning within the field of power electronics. His primary research interests include power electronics and energy storage systems, focusing on the development, control, and monitoring of modular energy storage and conversion systems.

Pouyan Pourhadi Abkenar received the M.S. degree in power engineering from the University of Tehran, Tehran, Iran, in 2019. Since 2022, he has been working toward the Ph.D. degree in power electronics engineering with Technical University of Kaiserslautern, Kaiserslautern, Germany.

Since 2019, he has been a Research Assistant with the University of Tehran. His research interests include the design, modeling, and control of resonant converters, dc–dc converters, and renewable energy systems. His research interests include design, modeling, and control of renewable energy systems and reconfigurable battery systems.

Alexander Koehler received the B.Sc. and M.Sc. degrees in electrical engineering from the Technical University of Kaiserslautern, Kaiserslautern, Germany, in 2020 and 2022, respectively. He is currently working toward the Ph.D. degree in electrical engineering with the University of Kaiserslautern-Landau, Kaiserslautern, Germany.

His research interest includes primarily centered around voltage and power flow control in distribution grids.

Hui Wang (Member, IEEE) received the B.Eng. degree from Shandong University of Science and Technology, Qingdao, China, in 2014, the M.Eng. degree from Tianjin University, Tianjin, China, in 2017, and the Ph.D. degree from The University of Hong Kong, Hong Kong, in 2022, all in electrical and electronic engineering.

He is currently a Postdoctoral Fellow with the Department of Electrical and Computer Engineering, Duke University, USA, and also with the Department of Electrical and Computer Engineering, University of Kaiserslautern-Landau, Kaiserslautern, Germany. Before that, he was a Postdoctoral Fellow with the Department of Electrical and Electronic Engineering, The University of Hong Kong. His research interests include electric machines and wireless power transfer technologies.

Stefan M. Goetz (Member, IEEE) received the B.S. and M.S. degrees in electrical engineering from Technische Universitat Munchen (TU Muenchen), Munich, Germany, in 2007 and 2008, respectively, and the Ph.D. training in electrical engineering from TU Muenchen and Columbia University, New York, NY, USA.

He previously worked in the automotive industry in various positions and levels with a focus on electric drive trains, machines, power electronics, high-power chargers, grid integration and grid stabilization for chargers, and vehicle architecture. His research interests include high-quality, high-power, high-bandwidth electronics and magnetics for drive and medical applications, as well as integrative power electronics solutions for microgrids and electric vehicles.